Journal of Engineering Mathematics **41:** 221–235, 2001.

Computation of particle settling speed and orientation distribution in suspensions of prolate spheroids

ESA KUUSELA[1,2], KAI HÖFLER[2] and STEFAN SCHWARZER[2]
[1]*Helsinki Institute of Physics and Laboratory of Physics, Helsinki University of Technology, P.O. Box 1100, FIN-02015 HUT, Espoo, Finland (e-mail: ekuusela@rock.helsinki.fi)*
[2]*Institut für Computeranwendungen 1, Universität Stuttgart, 70569 Stuttgart, Germany (e-mails: kai@ica1.uni-stuttgart.de; sts@ica1.uni-stuttgart.de)*

Received 26 June 2000; accepted in revised form 30 June 2001

Abstract. A numerical technique for the dynamical simulation of three-dimensional rigid particles in a Newtonian fluid is presented. The key idea is to satisfy the no-slip boundary condition on the particle surface by a localized force-density distribution in an otherwise force-free suspending fluid. The technique is used to model the sedimentation of prolate spheroids of aspect ratio $b/a = 5$ at Reynolds number 0·3. For a periodic lattice of single spheroids, the ideas of Hasimoto are extended to obtain an estimate for the finite-size correction to the sedimentation velocity. For a system of several spheroids in periodic arrangement, a maximum of the settling speed is found at the effective volume fraction $\phi(b/a)^2 \approx 0{\cdot}4$, where ϕ is the solid-volume fraction. The occurence of a maximum of the settling speed is partially explained by the competition of two effects: (i) a change in the orientation distribution of the prolate spheroids whose major axes shift from a mostly horizontal orientation (corresponding to small sedimentation speeds) at small ϕ to a more uniform orientation at larger ϕ, and (ii) a monotonic decrease of the the settling speed with increasing solid-volume fraction similar to that predicted by the Richardson–Zaki law $\propto (1-\phi)^{5{\cdot}5}$ for suspensions of spheres.

Key words: ellipsoids, finite differences, fibers, particle-scale simulation, sedimentation, spheroids, suspensions

1. Introduction

Understanding the hydrodynamically coupled motion of rigid bodies suspended in a fluid is an extremely complex and challenging endeavor. The problem has numerous applications in technology and is ubiquitous in nature, including particle motion in fluidized beds for reaction and combustion, sedimentation for separation or reaction in catalytic reactors, pneumatic and sediment transport, the rheological behavior of pastes and complex fluids, erosion, etc. In spite of the vast literature on the phenomena that occur in these systems, many fundamental questions are still open.

In this paper, we consider suspended rigid particles that are sufficiently large and consequently neglect Brownian motion. The motion of the suspending fluid is governed by the Navier–Stokes equations, subject to the no-slip boundary conditions at the surface of the suspended particles. We demonstrate how to obtain the force and torque exerted on the particles, and use them to find the particle trajectories via Newton's equations of motion.

Analytical results for particle motion require simplifying assumptions. For sufficiently slow flows – more precisely when both the Reynolds number of the flow and the Stokes number of the suspended particles are small – fluid and particle inertia are negligible. In this limit, the Navier-Stokes equations reduce to the linear Stokes equations. It is then possible to relate the forces and torques on all particles linearly to their linear and angular velocity by

either a resistance or a mobility tensor which only depends on the instantaneous geometry of the assembly. Jeffrey and Onishi [1] presented comprehensive results for the resistance and mobility functions of two unequal spheres in unbounded fluids. Batchelor [2] determined the average sedimentation velocity for randomly arranged equal-sized spheres at small solid-volume fractions ϕ to be $V_{\mathrm{St}}(1 - 6{\cdot}55\phi + O(\phi^2))$, where V_{St} is the Stokes sedimentation velocity of a single sphere.

For concentrated systems of many spheres, the Stokesian-dynamics simulation technique [3, 4] constructs the resistance tensor essentially as the sum of an approximate tensor capturing the effects of the hydrodynamic far field and the resistance tensor in a two-body lubrication approximation which captures the near field. Stokesian dynamics and closely related techniques [5, 6] demonstrate their capabilities in determining transport coefficients and structure formation in sheared suspensions [7] or sedimentation [5] of spherical particles. A comprehensive summary of different numerical techniques and analytical results was presented by Kim and Karrila [8, Parts III and IV].

For non-spherical particles, far fewer results are available. Jeffery [9] showed that ellipsoids execute closed trajectories in the orientation space, known as Jeffery orbits. He obtained analytical expressions for the orientation of the ellipsoid when one of the main axes is aligned to the vorticity vector of the shear flow. Lamb [10, pp. 604–605] presented the resistance of an ellipsoid with one of the main axes aligned with the direction of motion in infinitely extended flows. Analytical results for the volume-fraction dependence of the sedimentation-velocity statistical ensembles of sedimenting ellipsoids have not been derived.

Interest in the study of ellipsoids stems from the rheological properties of fiber suspensions. In the limit of very large aspect ratios, a suspension of spheroids is expected to show rheological properties very similar to those of suspensions of cylindrical fibers. Such suspensions are encountered, *e.g.*, in the production of paper and in the processing of fiber reinforced resins. Fiber suspensions show a pronounced enhancement of viscosity in extensional flows [11]. Moreover, a clustering instability has been observed to enhance the sedimentation speed in experiments [12, 13] and approximate dynamical simulations [14] beyond the values possible for single particles. Accordingly, there is considerable interest in the developement of mathematical and numerical methods that provide insight into the microstructure of flows involving many strongly interacting particles of elongated shape. For Stokes flows, Claeys and Brady [15, 16] extend the Stokesian dynamics method to prolate spheroids in three-dimensional flows and study the short-time limit of the hydrodynamics of prolate spheroid suspensions, but not the time evolution of the suspension microstructure. Mackaplow and Shaqfeh [14] have used the slender-body approximation in Monte-Carlo simulation of static fiber assemblies and point-particle approximations for the dynamical simulation of fiber suspensions, as will be discussed later in this paper.

In the Stokesian dynamics and boundary-integral methods, one exploits the linearity of the Stokes equations to formulate the quasi-stationary problem in terms of the particle degrees of freedom only. Larger particles imply larger sedimentation velocities and thus a larger particle Reynolds number. If either the particle or the container Reynolds number approaches one, we can no longer employ linearity or stationarity. A full spatial-temporal representation of the fluid flow has proved to be the most convenient numerical formulation. For example, Sugihara-Seki [17] considers the two-dimensional problem of one elliptical cylinder in channel flow in the absence of external forces and uses finite-element computations involving a spatial discretization adapted to the ellipse geometry. Feng and Joseph [18] extend previous work [19] on circular cylinders in 2D to elliptical cylinders, likewise using finite-element methods.

Numerical methods based on geometry-adaptive grid generation and repeated re-gridding in the course of the simulation demand extreme computational resources, in particular in three dimensions, and can thus only be applied to very small particle ensembles. Other authors approach the problem from a slightly different perspective and sacrifice some numerical accuracy for gains in computational efficiency by giving up geometrical adaptivity and using structured grids instead. Examples include the lattice Boltzmann [20, 21] and conventional techniques similar to finite differencing for the Navier–Stokes equation [22, 23, 24, 25].

In the following Section 2, we will summarize a technique presented in detail in Höfler and Schwarzer [23] that employs a structured grid to represent the fluid motion and uses ideas similar to the fictitious domain method of Glowinski *et al.* [24] and the immersed boundary technique [26] to simulate sedimenting systems of prolate spheroids. Its salient feature is the numerically convenient and efficient approach to implement the no-slip boundary condition on the particle surface in combination with a conventional flow solver. The total effort of implementation is comparable to that of a lattice-Boltzmann technique. In the form presented here, the simulation technique is appropriate for statistically homogeneous suspensions at particle volume fractions in the range of $\approx 0{\cdot}005 \ldots 0{\cdot}15$.

2. The marker technique

We describe the fluid motion by the dimensionless momentum equation,

$$\frac{\mathrm{D}}{\mathrm{D}t}\boldsymbol{u} = \boldsymbol{\nabla}\cdot\boldsymbol{T} + \tilde{\boldsymbol{f}}, \tag{1}$$

where $\frac{\mathrm{D}}{\mathrm{D}t}$ is the material derivative and all variables are nondimensionalized by use of the half minor axis a of the suspended spheroids, the fluid density ρ and the Stokes settling velocity

$$V_{\mathrm{St}} = \frac{2}{9}\frac{(\rho_p - \rho)ga^2}{\eta}, \tag{2}$$

which is the asymptotic sedimentation velocity for an isolated sphere with density ρ_p and radius a in an infinitely extended fluid with density ρ and shear viscosity η under the action of gravity g in the $-z = -x_2$ direction. The tensor $\boldsymbol{T}$ is the Newtonian stress tensor, $T_{ij} = -\tilde{p}\delta_{ij} + (1/\mathrm{Re})[(\partial/\partial x_i)u_j + (\partial/\partial x_j)u_i]$, while $\tilde{\boldsymbol{f}}$ denotes the volume-force density. The Reynolds number is defined as $\mathrm{Re} = aV_{\mathrm{St}}\rho/\eta$. We have assumed constant fluid density which implies incompressibility, thus $\boldsymbol{\nabla}\cdot\boldsymbol{u} = 0$. The divergence of the stress tensor then reads $\boldsymbol{\nabla}\cdot\boldsymbol{T} = -\boldsymbol{\nabla}\tilde{p} + (1/\mathrm{Re})\nabla^2\boldsymbol{u}$. It is computationally convenient to cancel the gravitational contribution $-ga/V_{\mathrm{St}}^2\boldsymbol{e}_z$ to $\tilde{\boldsymbol{f}}$ against the hydrostatic pressure $-gaz/V_{\mathrm{St}}^2$. We introduce the symbols p and $\boldsymbol{f}$ to denote the remaining dynamic contributions to the pressure and the volume force terms, respectively. With these conventions, we obtain the Navier-Stokes equations,

$$\frac{\mathrm{D}}{\mathrm{D}t}\boldsymbol{u} = -\boldsymbol{\nabla}p + \frac{1}{\mathrm{Re}}\nabla^2\boldsymbol{u} + \boldsymbol{f}, \tag{3}$$

accompanied by the incompressibility constraint $\nabla\cdot\boldsymbol{u} = 0$. We discretize Equation (3) on a regular, staggered marker-and-cell (MAC) mesh to second-order precision in space (*cf.*, *e.g.*, [27]). For the time stepping, we employ an operator-splitting-technique which is explicit and accurate to first order: A term $\boldsymbol{u}^*$ is added and subtracted on the left-hand side of Equation

(3), which permits a split of (3) into a system of two equations for the discretized variables $\boldsymbol{u}^n$, p^n and $\boldsymbol{f}^n$,

$$\frac{\boldsymbol{u}^* - \boldsymbol{u}^n}{\Delta t} = -(\boldsymbol{u}^n \cdot \boldsymbol{\nabla})\boldsymbol{u}^n + \frac{1}{\mathrm{Re}}\nabla^2 \boldsymbol{u}^n + \boldsymbol{f}^n, \tag{4}$$

$$\frac{\boldsymbol{u}^{n+1} - \boldsymbol{u}^*}{\Delta t} = -\nabla p^{n+1}. \tag{5}$$

Here, Δt denotes the time step and the superscript n the time $t = n\Delta t$. From the first equation, we determine $\boldsymbol{u}^*$, subject to periodic boundary conditions. Taking the divergence of the second equation and using the incompressibility condition $\boldsymbol{\nabla} \cdot \boldsymbol{u}^n = 0$, we find a Poisson equation for the pressure which we solve by means of a multigrid method[1]. Finally, we employ Equation (5) to find the updated velocity field $\boldsymbol{u}^n$. More details of the solution procedure are described in [23]. Due to the simple and static data structures, the solver requires only little storage and is straightforward to parallelize. The multigrid algorithm ensures that the computational effort is proportional to the number of grid points when we increase the system size, while keeping the grid spacing constant.

The challenge is to incorporate the suspended ellipsoids into the fluid description so as to (i) satisfy the no-slip boundary condition on the particle surface without compromising the efficiency of the fluid solver, and (ii) calculate the forces $\boldsymbol{F}_i^f$ and torques $\boldsymbol{\tau}_i^f$ exerted by the fluid on particle i. Ideally, smooth particles should never touch due to the divergent lubrication forces on approach. However, on a finite grid, we cannot resolve this divergence and we must introduce additional forces $\boldsymbol{F}_i^p$ and torques $\boldsymbol{\tau}_i^p$, as will be described in detail later.

Newton's equation of motion for the center of mass of particle i reads

$$\dot{\boldsymbol{v}}_i = \frac{\boldsymbol{F}_i^f}{M_i} + \frac{\boldsymbol{F}_i^p}{M_i} - \frac{9}{2}\frac{\rho}{\rho_p}\frac{1}{\mathrm{Re}}\boldsymbol{e}_z, \tag{6}$$

where $\boldsymbol{v}_i$ is the velocity of the center of mass and M_i is the mass of particle i. The equation has been nondimensionalized as described for the fluid equation (1), leading to a mass scale of ρa^3 and a force scale of $\rho V_{\mathrm{St}}^2 a^2$. Prolate spheroids have a twofold degenerate minor axis a and a major axis b which leads to the dimensionless mass $M_i = (4/3)\pi(\rho_p/\rho)(b/a)$. Since we have removed the hydrostatic pressure from the fluid equations, we need to introduce a buoyancy term into the particle equations. Together with the weight of the particles, it forms the third term on the right-hand side of (6).

For the angular velocity $\boldsymbol{\omega}_i$ of the rigid particles, we obtain

$$\boldsymbol{I}_i \dot{\boldsymbol{\omega}}_i = \boldsymbol{\tau}_i^f + \boldsymbol{\tau}_i^p, \tag{7}$$

where the torques and angular velocity are computed with respect to the center of mass, and $\boldsymbol{I}_i$ is the inertia tensor of particle i.

Both the objectives (i) and (ii) mentioned above can be addressed at the same time. The general idea is to represent the rigid particles via a manipulation of the body force term $\boldsymbol{f}$

[1] We note that p^n in the numerical formulation presented above has some properties which are not shared with the physical pressure. For example, in the presence of a rigid boundary the numerical solution of the system (4–5) does not depend on the value of $\boldsymbol{u}^*$ on the boundary and we can thus choose any convenient value for the normal pressure derivative, typically 0 (*cf.* [27, pp. 143–207]). This freedom does not exist for periodic systems. Furthermore, p is not evaluated at the same 'time' as the diffusive and convective terms and thus it does not strictly correspond to the physical pressure field [28, pp. 623–627].

in (3). To this end, we consider $\boldsymbol{f}$ to be a spatially distributed (fictitious) constraint volume force which causes the fluid to move as a rigid body 'inside' the particles. Observed from the outside, the rigid body region imposes the same constraints as a true rigid particle at the same location, thus giving rise to the same stresses at the 'interface'. The no-slip condition is satisfied to the same degree as the equation of motion for the fluid and its discretization guarantees continuity. The forces and torques on the particles are equal to specific moments of the constraint force distribution, so that we can avoid the explicit integration of the stress over the particle surface which is otherwise necessary in order to compute F_i^f and $\boldsymbol{\tau}_i^f$.

In order to determine the fictitious body force numerically, we use an explicit penalization technique which integrates seamlessly with the fluid solver. First, we introduce rigid particle 'templates' T_i of the same shape as the physical particle i. For each T_i we define a displacement field $\boldsymbol{\epsilon}_i(\boldsymbol{x})$, for all $\boldsymbol{x} \in T_i$. We identify the position of the T_i's center of mass by $\boldsymbol{x}_i$. Numerically, we choose a finite number of reference points $\boldsymbol{x}_{ij}^r$ on T_i, $j = 1, \ldots N_i$ to which we 'attach' the field $\boldsymbol{\epsilon}_i(\boldsymbol{x}_{ij}^r)$. The reference points associated with any one template i maintain the same relative positions, following the T_i's rigid body translation and rotation

$$\boldsymbol{x}_{ij}^r = \boldsymbol{x}_i + \boldsymbol{O}_i(t) \cdot \boldsymbol{r}_{ij}. \tag{8}$$

The constant vectors $\boldsymbol{r}_{ij}$ denote the initial position of the reference points with respect to the center of mass of T_i. The rotation matrix $\boldsymbol{O}_i(t)$ describes the instantaneous orientation of T_i. In order to define the displacement field $\boldsymbol{\epsilon}_i$, we associate with each reference point ij a fluid tracer at $\boldsymbol{x}_{ij}^m$, initially $\boldsymbol{x}_{ij}^m(0) = \boldsymbol{x}_i + \boldsymbol{r}_{ij}$, whose motion is determined by the local fluid velocity, *i.e.*,

$$\dot{\boldsymbol{x}}_{ij}^m = \boldsymbol{u}(\boldsymbol{x}_{ij}^m), \tag{9}$$

and define $\boldsymbol{\epsilon}_i(\boldsymbol{x}_{ij}^r) = \boldsymbol{x}_{ij}^m - \boldsymbol{x}_{ij}^r$ for all reference points ij.

We now choose the force density $\boldsymbol{f}^c$ arising due to the displacements $\boldsymbol{\epsilon}_i$ to be

$$\boldsymbol{f}_i^c(\boldsymbol{x} + \boldsymbol{\epsilon}_i(\boldsymbol{x})) = -k'\boldsymbol{\epsilon}_i(\boldsymbol{x}), \tag{10}$$

which can be interpreted as a spring connecting the tracer and the reference point. The force density $\boldsymbol{f}_i^c$ is zero in the exterior of the region $\Omega_i = \{\boldsymbol{x} + \boldsymbol{\epsilon}_i(\boldsymbol{x}),\ \boldsymbol{x} \in T_i\}$ associated with template T_i. We impose the force density $\boldsymbol{f}_i^c$ onto the fluid by interpolation to the six nearest grid points. Its sign ensures that the effect on the fluid will tend to be a reduction of the modulus of $\boldsymbol{\epsilon}_i$. If the external stresses are bounded, then $\boldsymbol{\epsilon}_i$ remains bounded and approaches zero as the spring constant k' increases. If k' is sufficiently large then the internal time scale associated with building up the reaction force is short compared to the physical time scale a/V_{St} which determines how fast the fluid velocity can change. On time scales longer than a/V_{St} we can thus consider the no-slip boundary condition as being satisfied.

The templates T_i also serve to include the inertial contributions of the physical particles which arise when particle and fluid densities differ. We define M_i^f as the fluid mass 'inside' the particle and the 'missing' mass $M_i^t = M_i - M_i^f$. The templates then execute rigid body motion according to the equation of motion,

$$M_i^{\mathrm{t}}\dot{\boldsymbol{v}}_i = \boldsymbol{F}_i^f + \boldsymbol{F}_i^p - \frac{9}{2}M_i^{\mathrm{t}}\frac{\rho}{\rho_p}\frac{1}{\mathrm{Re}}\boldsymbol{e}_z + \boldsymbol{F}_i^c. \tag{11}$$

The forces $\boldsymbol{F}_i^f$ and $\boldsymbol{F}_i^p$ as well as the buoyancy and weight term are the same as those introduced in Equation (6). The force $\boldsymbol{F}_i^c$ is the 'reaction' to the fictitious body force and is defined as the negative integral of $\boldsymbol{f}_i^c$ over Ω_i.

We note that, by itself, due to the different mass and additional force term $\boldsymbol{F}_i^c$, Equation (11) is *not* equivalent to the particle equation of motion (6). Also, for neutrally buoyant particles the inertial term in (11) vanishes and we must instead compute the template position (which appears implicitly in $\boldsymbol{F}_i^c$) directly from a force and torque equilibrium.

We find the total rate of change of momentum $\dot{\boldsymbol{P}}_i^f$ of the fluid 'inside' the particle by integration of (3) over Ω_i, letting $\boldsymbol{f} = \boldsymbol{f}_i^c$,

$$\dot{\boldsymbol{P}}_i^f = \oint_{\partial\Omega_i} \boldsymbol{T} \cdot \mathrm{d}\boldsymbol{A} - \boldsymbol{F}_i^c, \tag{12}$$

where we have made use of the definition of $\boldsymbol{F}_i^c$ and Gauß's theorem to convert the volume integral over the divergence of the stress into a surface integral. For incompressible fluids, $\dot{\boldsymbol{P}}_i^f$ is proportional to the rate of change of the center of mass velocity of the fluid in Ω_i, *i.e.*, $\dot{\boldsymbol{P}} = M_i^f \dot{\boldsymbol{v}}_i^{CM}$, The value $1/k'$ sets the degree of accuracy up to which Ω_i resembles the template T_i and thus the shape of the physical particle.

Adding the equation of motion of the template (11) and of Ω_i [Equation (12)], we see that the internal constraint forces $\boldsymbol{F}_i^c$ cancel, leaving only external forces

$$(M_i^t + M_i^f)\dot{\boldsymbol{v}}_i = M_i \dot{\boldsymbol{v}}_i = \oint_{\partial T_i} \boldsymbol{T} \cdot \mathrm{d}\boldsymbol{A} + \boldsymbol{F}_i^p - \frac{9}{2}(M_i^t + M_i^f)\frac{\rho}{\rho_p}\frac{1}{\mathrm{Re}}\boldsymbol{e}_z. \tag{13}$$

To the degree that the penalization guarantees that Ω_i has the shape of the modeled particle, the surface integral occurring in Equation (12) is equal to the hydrodynamic force $\boldsymbol{F}_i^f$ of Equation (6) for the physical fluid-particle interaction. Dividing by M_i we thus recover the equation of motion (6) for a rigid particle suspended in the fluid.

The arguments above can be repeated for the angular motion. Considering the ith template to have a moment of inertia $I_i^t = I_i - I_i^f$, we demand

$$I_i^t \dot{\boldsymbol{\omega}}_i = \boldsymbol{\tau}_i^f + \boldsymbol{\tau}_i^p + \boldsymbol{\tau}_i^c, \tag{14}$$

where the torques $\boldsymbol{\tau}_i^\alpha$ refer to the fluid ($\alpha = f$), the particle contact ($\alpha = p$), and for $\alpha = c$ to the integral of $\boldsymbol{r}_i \times \boldsymbol{f}_i^c$. In analogy to (12) we obtain the total hydrodynamic torque on the 'inside' fluid if we operate with $\boldsymbol{r}_i \times$ on the momentum equation (12) and then integrate over Ω_i. Adding the resulting equation to (14), the torques due to the constraints cancel in the limit of large k' and we recover the relation for the angular motion of the particle (7).

We must still specify the force $\boldsymbol{F}_i^p$ due to particle-particle contacts. At sufficiently low Reynolds numbers, we know from lubrication theory that the presence of the fluid prevents smooth particle surfaces from touching. At very small distances, when particles approach one another on a path perpendicular to their surface at a fixed velocity, the stresses necessary to displace the fluid are inversely proportional to the distance of the surfaces. These forces are captured correctly only on scales larger than the grid resolution. Since we will here work with dilute systems in terms of particle-volume fraction, we consider close particle encounters to be rare. We thus do not attempt to model lubrication forces, but introduce an elastic restoring force which prevents significant particle overlaps. From our experience with suspensions of spheres [23], we think that lubrication effects are not important for the collective settling behavior up to particle-volume fractions of $\approx 0{\cdot}15$

The force between two colliding particles is taken to be proportional to the amount of their mutual virtual overlap. For non-overlapping particles this force is set to zero. As a further

justification for using the elastic particle-particle interaction, we can assume that the short-range diverging lubrication forces deliver the elastic behavior of the particles even if they are not in true contact. We have employed the method described by Perram *et al.*[29, 30], who define a contact function

$$C_{ij} = \max\left\{4\lambda(1-\lambda)\boldsymbol{X}_{ij}^T\boldsymbol{G}_{ij}^{-1}(\lambda)\boldsymbol{X}_{ij}|\lambda \in [0,1]\right\}. \tag{15}$$

for two ellipsoidal bodies i and j. Here, $\boldsymbol{X}_{ij} = \boldsymbol{x}_i - \boldsymbol{x}_j$ is the distance between the centers of mass of the ellipsoids, and the matrix $\boldsymbol{G}_{ij}(\lambda)$ is defined as

$$G_{ij}(\lambda) = (1-\lambda)(\boldsymbol{O}_i^T\boldsymbol{R}_i^2\boldsymbol{O}_i)^{-1} + \lambda(\boldsymbol{O}_j^T\boldsymbol{R}_j^2\boldsymbol{O}_j)^{-1}. \tag{16}$$

The diagonal matrix $\boldsymbol{R}_i$ contains half the axes of the respective ellipsoid i. At contact the function C_{ij} is unity and lower values indicate overlap. The chosen contact function is not isotropic for large particle separations, but this causes no problem, since we set the force to zero for non-overlapping particles.

Finally, we note that for all methods that use fixed structured grids the accessible maximum system size is limited by the available computational resources. Since the grid spacing must be smaller than the particle size, there is also a practical lower limit for the particle-volume fraction, typically in the range of fractions of one percent. Adapted grids will be appropriate for strongly inhomogeneous suspensions or complex geometries, but there are no conceptual difficulties applying the ideas presented above to those cases.

3. Results

We now use the described algorithm to study a sedimenting periodic lattice of spheroids and compare the results to the analytical solution for one isolated sedimenting spheroid corrected approximately for the effects of the periodicity (Section 3.1). We will then discuss statistical properties of a periodical system of a set of spheroids, in particular the mean settling velocity and its relation to the orientation distribution as functions of the volume fraction (Section 3.2).

3.1. A SINGLE ELLIPSOID

We test our algorithm for the case of one spheroid with aspect ratio $b/a = 5$ and minor half axis a sedimenting in a periodically repeated cubic unit cell with edge $L = 20$. In the computation, the grid spacing is $h = 0{\cdot}625$. We model the shape of the spheroid using 133 tracer and reference points. Unless otherwise stated, the particle Reynolds number is 0·3.

The spheroid is initially at rest and positioned at an angle β subtended by the major axis and the vertical, varying between 0 and $\pi/2$. At vanishing Reynolds numbers, due to the time reversibility of Stokes flow, the particle will maintain its orientation. At finite Re, the flow field exerts a torque that tends to turn the particle to the horizontal direction. The angular speed increases with Re. This observation is in accordance with results of the simulation of elliptical cylinders at sufficiently wide channel geometries and low, but non-zero Reynolds numbers [22, 25, 31]. For very narrow channels and sufficiently slow settling, however, Huang *et al.* [31] report that an ellipse will turn its major axis into the vertical direction.

In order to facilitate a comparison with analytical results [32, pp. 219–232] for the sedimentation velocity and the horizontal drift, we prevent angular motion of the particle, *i.e.*, we keep β equal to its initial value and repeat the simulation for several values of β. The resulting sedimentation velocity components are plotted in Figure 1.

The analytical results for spheroids in infinitely extended systems at $\mathrm{Re} = 0$ show a sinusoidal variation of the horizontal velocity,

$$v_x = \frac{3}{16}\frac{A}{(A^2-1)^{3/2}}\left(3A\sqrt{A^2-1} + (2A^2-3)\log(A+\sqrt{A^2-1}) + (1-2A^2)\log\frac{A+\sqrt{A^2-1}}{A-\sqrt{A^2-1}}\right)\sin 2\beta, \tag{17}$$

where $A = b/a$ and log is the natural logarithm. The vertical velocity

$$v_z = \frac{3}{16}\frac{A}{(A^2-1)^{3/2}}\left[\left(A\sqrt{A^2-1} + (3-2A^2)\log(A+\sqrt{A^2-1}) + (1-2A^2)\log\frac{A+\sqrt{A^2-1}}{A-\sqrt{A^2-1}}\right) + \left(3A\sqrt{A^2-1} + (2A^2-3)\log(A+\sqrt{A^2-1}) + (1-2A^2)\log\frac{A+\sqrt{A^2-1}}{A-\sqrt{A^2-1}}\right)\cos 2\beta\right] \tag{18}$$

shows a variation proportional to $\cos 2\beta$ around an orientation-independent value. Despite the non-zero Reynolds number, in our simulation in periodic cells, the dependence on angle and the amplitude of the variations are almost the same as the theoretical predictions for Stokes flow. The measured vertical average sedimentation velocity, however, shows a pronounced offset from the infinite system, $\mathrm{Re} = 0$ result which we now address.

In order to obtain an estimate of the necessary corrections to account for the periodicity of the system, we resort to the approach of [33] who computed the drag in a periodic lattice of spheres. Hasimoto replaces the exact flow field by the appropriate fundamental solution of the Stokes equation *in periodic lattices* expressing a point force with volumetric flow rate v_z. To obtain an expression for the source strength, and thus the negative drag on one of the spheres, he employs an approximation attributed to Burgers. The source strength is calculated from the condition that the integral of the velocity *of the fundamental solution* over the surface of any one of the spheres in the array shall vanish [Equation (4.5) in his paper], a condition which also holds true for the *exact* solution obeying the no-slip condition. Since the fundamental solution captures the flow properties far from extended bodies, Hasimoto's approach recovers the drag for large values of L/a or for small volume fractions of spheres.

If we equate the negative drag to the weight of a sphere in the stationary case, then v_z can be interpreted as the sedimentation velocity of a lattice of spheres. We now employ Hasimoto's approach as described above to estimate the sedimentation velocity of a periodic array of sedimenting spheroids. We determine the source strength for the fundamental solution such that the surface integral of the velocity field over the surface of a spheroid, with given value of A and β, vanishes. This strength will in general be directed neither along the major axis nor in z direction; it is, however, linearly dependent on v_z. Setting the strength to the weight of the spheroids ($A = 5$), we obtain, for example, $v_z = -3{\cdot}01 + 14{\cdot}19(a/L)$ if the main axis is aligned with gravity ($\beta = 0$) and $v_z = -2{\cdot}37 + 14{\cdot}19(a/L)$] for $\beta = \pi/2$. A Maple worksheet to compute v_z for other values of A and β is available on request from the authors. We stress that, even in the limit of small volume fractions, for $A \neq 1$, these solutions cannot be expected to become exact, because we make a systematic error arising from the use of the approximate

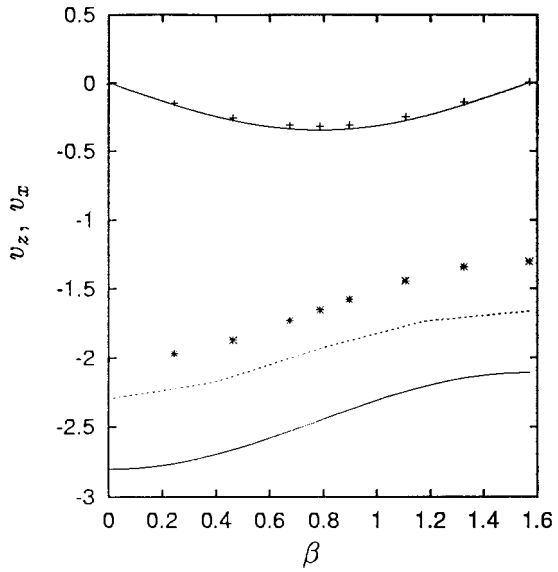

Figure 1. Sedimentation velocity of a single sedimenting particle ($b/a = 5$, Re $= 0{\cdot}3$) in a periodically repeated simulation cell of size $20 \times 20 \times 20$ shown as a function of the angle β between major axis and direction of gravity. The angle is held fixed during the sedimentation process. Single points correspond to the simulation results, whereas solid lines are the Stokes-regime predictions for particles in unbounded fluids. There is almost no difference in the horizontal drift velocity v_x (upper part), but a significant offset for the velocity component in the vertical direction v_z. Plotted for comparison, the dotted line shows the results for the expected vertical sedimentation velocity for a periodic array of particles following from an extension of Hasimoto's [33] arguments to spheroids. We do not expect the simulation results to match this line exactly, because the underlying assumptions are valid only in the limits $b/a \to 1$, Re $\to 0$ and to order a/L, but the difference demonstrates clearly the importance of finite-size effects.

fundamental instead of the full solution of the Stokes equation. The error increases with the aspect ratio A. The dotted line in Figure 1 shows the expected sedimentation velocity for periodic dilute suspensions from our use of Hasimoto's arguments for $a/L = 20$ and $A = 5$.

As compared to the analytical single-particle result, significant finite-size corrections are visible. We think that most of the remaining deviation is due to our approximation of the flow field and the crude treatment of the no-slip boundary conditions. Further contributions of unknown but probably smaller amplitude are due to the finite Reynolds number, which likewise tends to lower the sedimentation speed, and finally the resolution of the computational grid. In accordance with the analytical prediction for Stokes flow, the single fiber sediments fastest when oriented vertically ($\beta = 0$) and slowest when oriented horizontally ($\beta = \pi/2$).

3.2. Settling speed in suspensions of spheroids

We now turn to discussing the case of many suspended particles. Due to their ability to transmit stress instantaneously along their long axis b, rigid elongated objects influence regions of the flow of dimension b^3. Thus, in comparison with suspensions of spheres, suspension of high-aspect-ratio fibers, with minute volume fractions ϕ, suffice to produce significant hydrodynamic effects. We thus follow the common practice and multiply the spheroid volume fraction by $b^3/ba^2 = (b/a)^2$ to allow for better comparison of our results with other studies of fiber or ellipsoid suspensions with aspect ratios that differ from the one considered here. The concentration range with $\phi(b/a)^2 > 1$ and $\phi \ll 1$ is called the semi-dilute regime.

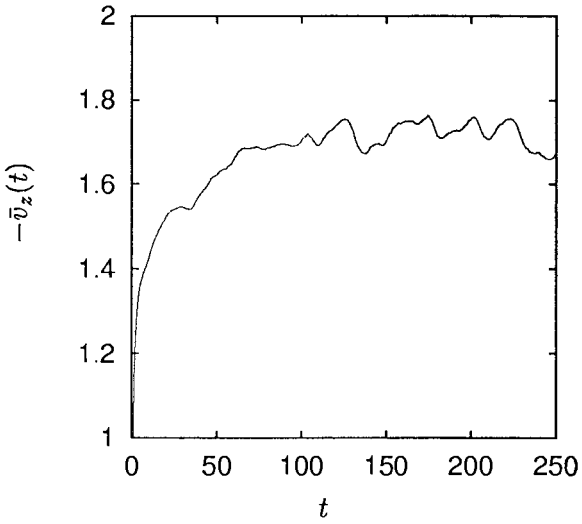

Figure 2. Negative of the sedimentation velocity $-\bar{v}_z(t)$ averaged over particles in 20 different initial configurations as a function of time.

In the same geometry as used above, we now release a few ellipsoids at random positions and with random orientation. The positions and orientations now vary in accordance with the stresses induced by the fluid motion.

The approach of the suspension dynamics to a steady state is demonstrated by the time evolution of the sedimentation velocity of the particles during the initial phase of the simulation (Figure 2). The velocities have been averaged over 20 simulations and the used volume fraction is $\phi(b/a)^2 = 1$. The average particle velocity continues to increase during a long transient period, and after 100–150 Stokes times it becomes stationary. In the steady state, we still observe fluctuations of the temporary average velocity, but no long-term drift. Hereafter, we concentrate on the steady-state behavior. All averages are taken as time, particle and ensemble averages starting after the initial transient behavior has ended.

Next, we study the average particle velocity. The horizontal components of the average velocity approach zero. The resulting average velocity component in the vertical direction is displayed in Figure 3. Entering the semi-dilute from the dilute regime $\phi(b/a)^2 \ll 1$, we first pass through a maximum of the sedimentation velocity at $\phi(b/a)^2 \approx 0{\cdot}4$ before we observe a monotonic decrease. The existence of this maximum is quite remarkable, since it is not present in suspensions of spherical particles. The experiments of Herzhaft and Guazzelli [13] suggest a maximum in the sedimentation velocity for *cylindrical* fibers with $A = 5,\ 11$ and 32 at a value of $\phi \approx 5 \times 10^{-3}$ independent of A within the experimental error bars. This value is lower than that observed in the spheroid simulations (0·016).

The experimentally observed maximum settling velocity for $A = 5$ and $A = 11$ is larger than that for a single, vertically oriented fiber and thus cannot be explained by a concentration dependence of fiber orientation alone. Koch and Shaqfeh [34] described an instability mechanism that leads to cluster formation in dilute fiber suspensions at low Reynolds numbers. A 'test' fiber in the velocity field far from a sedimenting single fiber tends to orient its main axis such that the relative velocity of the two particles becomes negative. Thus, the fibers will tend to form clusters until near-field effects or contact forces intervene. In simulations at $\mathrm{Re} = 0$ that use a point-particle approximation and neglect lubrication effects, at much lower effective

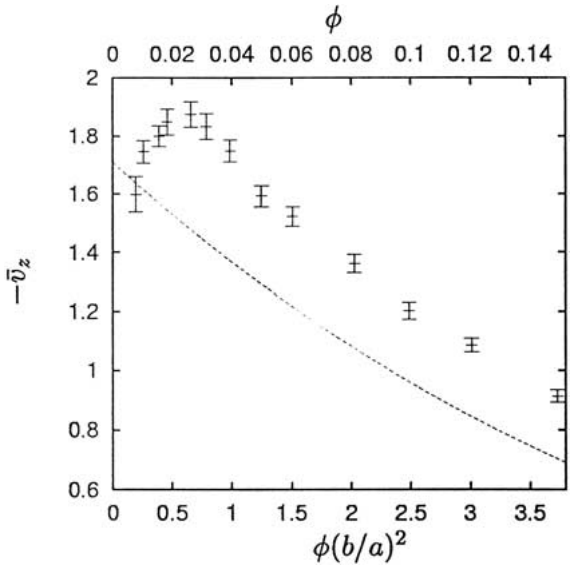

Figure 3. Negative of the average sedimentation velocity $-\bar{v}_z$ of a suspension of spheroids as a function of the effective volume fraction $\phi(b/a)^2$. The dotted curve shows the Richardson–Zaki law $(1-\phi)^{5{\cdot}5}$ multiplied by the velocity expected for a dilute suspension with the same orientation distribution for the particles than measured in our case for large effective volume fractions. Corresponding true volume fractions ϕ are marked on the top axis. Error bars denote statistical errors of the mean from averaging over initial conditions and time.

volume fraction 0·1 and higher aspect ratio ($A = 100$), Mackaplow and Shaqfeh [14] have observed fiber clustering to the extent of streamer formation in the simulation cell. In these simulations, no stationary sedimentation velocity was observed by the end of the simulations after 100–200 Stokes times. The strong increase in sedimentation velocity could only be attributed to cluster formation.

Visual inspection of the simulated particle arrangement reveals a non-uniform distribution of fibers after the transient, but the simulated suspension sedimentation velocity never exceeds possible single fiber values. We know that, unlike in Stokes flow, single, unconstrained fibers turn horizontal and sediment slowly compared to fibers in vertical orientation. As the concentration increases, we expect hydrodynamic interactions with other particles to destabilize the horizontal state. Thus, for low volume fractions the dimensionless sedimentation speed should be smaller than in inertia-free flows.

In order to assess the importance of the orientation distribution, we next focus on the distribution $n(\cos\beta)$ of the cosine of the 'polar' angle of the major axis with the vertical, where $n(\cos\beta)\sin\beta d\beta$ is the fraction of particles with polar angles in the range $\beta \ldots \beta + d\beta$; $n(\cos\beta)$ equals 1 for particle orientations distributed uniformly over the unit sphere. Our numerical findings, averaged over several initial configurations and simulation time, are displayed in Figure 4.

Herzhaft *et al.* [12, 13] find that the orientation distribution is almost independent of aspect ratio. They measure the angles from the projected images in the *xy*-plane. These cannot be directly compared to the vertical angles β, but their results imply that a fraction of more than half of the fibers have $\cos\beta > 0{\cdot}9$ [13]. Since inertia in otherwise undisturbed flows tends to align fibers horizontally, in our simulations the orientation distribution at low $\phi(b/a)^2$ shows a significant fraction of horizontally oriented spheroids. For $\phi(b/a)^2 = 0{\cdot}263$, even the

maximum is located at $\cos\beta = 0$. Only for $\phi(b/a)^2 > 0{\cdot}4$ the maximum appears at $\cos\beta = 1$, corresponding to vertical alignment. Increasing the concentration further does not alter the distribution significantly, although the maximum of the distribution at $\cos\beta = 1$ continues to increase slightly.

Clusters of sedimenting fibers experience shear forces where particles are exposed to the back-flow in their environment. Thus, we expect these particles to follow trajectories (flips) reminiscent of Jeffery orbits, *i.e.*, the particle rotates as dictated by the vorticity of the flow, but for long times remains oriented with its major axis in the shear plane, in our case parallel to gravity, and then rapidly flips by an angle of π into the opposite direction. Such flips have been observed in fiber suspensions [12, 13] and in the simulations by Mackaplow and Shaqfeh [14].

It is instructive to examine what the orientation distribution would be if all fibers followed Jeffery orbits. Let us assume that the flow vorticity points in the positive y direction. The Jeffery orbit of the particle is then governed by

$$\dot{\beta} = \kappa \frac{A^2 \cos(\beta)^2 + \sin(\beta)^2}{A^2 + 1}, \tag{19}$$

where κ denotes the shear rate. The inverse of the angular velocity is proportional to the probability of finding the particle at a random instant with orientation β. That is to say, for an ensemble of independent particles following Jeffery orbits, we find $n_J(\beta) \propto 1/\dot{\beta}$ as the probability density for any one of them to have orientation β. It is, however, more convenient to work with the probability $n_J(cos\beta)$ of finding a specific value of $\cos\beta$, because a geometrically random distribution of orientations β corresponds to $n(\cos\beta) = 1$. We use $n_J(\beta)\mathrm{d}\beta = n_J(\cos\beta)\mathrm{d}\cos\beta$ and take the normalization into account. Then we find,

$$n_J(\cos\beta) = \left(\int_0^{\pi/2} \frac{\mathrm{d}\beta}{A^2 \cos(\beta)^2 + \sin(\beta)^2} \right)^{-1} \frac{1}{\sin(\beta)} \frac{1}{A^2 \cos(\beta)^2 + \sin(\beta)^2}. \tag{20}$$

The distribution is independent of the shear rate κ of the flow. The normalization integral in this expression can be computed analytically, and for $A = 5$ is found to be $(13/5)\pi$.

Like the measured orientation distribution, the distribution n_J increases with β. The inverse sine factor causes an inverse square root singularity in $1-\cos\beta$ as $\cos\beta \to 1$, *i.e.* for the major axis lying in the shear plane.

In a three-dimensional suspension, the situation is more complex. The flow in general displays an elongational component in addition to non-planar shear profiles and local variations in shear rate. Even in plane shear, the major axis of the fibers precesses on a cone with axis in the direction of vorticity and if we assume that shear mostly appears in the vertical velocity components, β will then not assume its extreme values 0 or $\pi/2$. However, the simulated stationary orientation distributions show a maximum at $\cos\beta = 1$, reminiscent of the inverse-square-root singularity expected in the ideal case.

The behavior of the sedimentation speed at large concentrations is monotonically decreasing, analogous to the behavior of sphere suspensions at low Reynolds numbers which are well described by the phenomenological Richardson–Zaki law $\bar{v}_z = (1-\phi)^n$, where $n \approx 5 \ldots 6$ for $\mathrm{Re} \to 0$. To see whether this law describes the behavior in the semi-dilute regime, we first estimate a value for the sedimentation speed from the assumption that fibers sediment independently, $\bar{v}_z^{(0)} = \int v_z(\cos\beta) n(\cos\beta)\mathrm{d}\cos\beta \approx -1{\cdot}71$. Here, we have used the measured single particle sedimentation velocities v_z from Figure 1 and the orientation distribution for $\phi(b/a)^2 = 3{\cdot}8$. We then plot the expression $\bar{v}_z^{(0)}(1-\phi)^{5{\cdot}5}$ in Figure 3; ϕ is indicated by

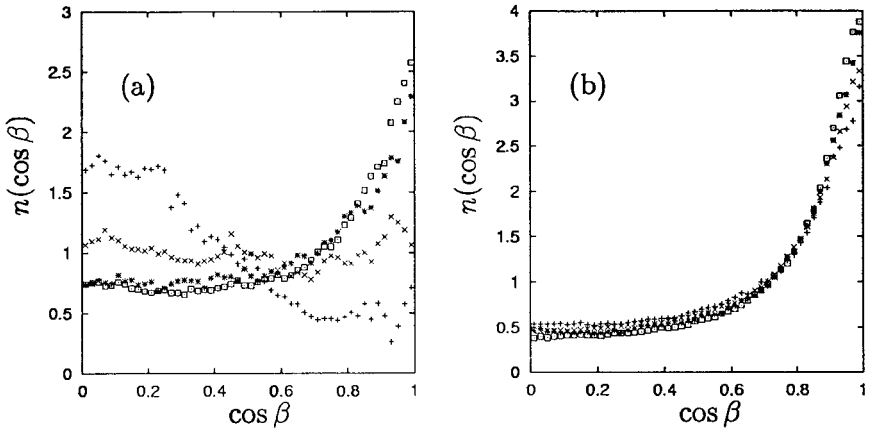

Figure 4. Distribution of cos(β) of particles sedimenting at effective volume fractions $\phi(b/a)^2 = 0{\cdot}263(+)$, $0{\cdot}393(\times)$, $0{\cdot}625(*)$, $0{\cdot}75(\square)$ in part (a) and at $\phi = 1{\cdot}5(+)$, $2{\cdot}3(\times)$, $3{\cdot}0(*)$, $3{\cdot}8(\square)$ in part (b) of the figure. Note that an entirely random orientation distribution of fibers corresponds to a constant of 1. Part (a) demonstrates that the distribution changes from one in which the particles prefer the horizontal direction that is typical for the single spheroid behavior to one in which the vertical direction is favored. The maximum of the sedimentation velocity is associated with the distribution $(\times)$ where the particles do not experience strong back-flow, but start to interact in such a fashion that a substantial fraction turns away from the horizontal to assume other orientations.

the labels on the upper axis. We see that the functional form of the settling velocity for effective volume fractions larger than for the maximum is reproduced quite well, and the hindrance effects seem to be captured well by the Richardson–Zaki correlation. However, the sedimentation speed is substantially larger than expected from the single-particle behavior which can be accounted for by clustering effects. To see whether this agreement is not purely coincidental, we must repeat the simulations with a different aspect ratio of the spheroids: it must then become clear, whether the large-ϕ behavior of the settling velocity scales with ϕ or rather with the effective volume fraction $\phi(b/a)^2$. A scaling with ϕ indicates that the reduction of the settling velocity is controlled by the average back-flow velocity, because its value $-v_z\phi/(1-\phi)$ is set by the real volume fraction and not by the effective one. We hope to address this interesting issue in the future.

4. Summary and conclusion

We have presented three-dimensional dynamical simulations of suspensions of sedimenting prolate spheroids at small, but nonzero Reynolds numbers. We observe a maximum of the sedimentation velocity as a function of the volume fraction of fibers at the volume fraction $\phi(b/a)^2 \approx 0{\cdot}4$. We also presented simulation data for the distribution of the orientation of the spheroids and linked their properties to the form of the sedimentation velocity curve. In the semi-dilute regime, the distribution of orientations does not change significantly, and the sedimentation velocity decreases monotonically due to the increasing back-flow. At low volume fractions, inertial effects tend to align particles horizontally and thus lead to a reduction in the sedimentation speed as compared to Stokes flow.

Acknowledgements

We thank the numerous present and former colleagues at the Institute for Computer Applications whose programming expertise helped and still helps to implement the public simulation library on which the simulation program is built (http://www.ica1.uni-stuttgart.de/Research). We also appreciate the responsiveness of Elizabeth Guazzelli who patiently answered our questions concerning the physics of fiber suspensions and the discussions with Tapio Ala-Nissila and Jason Butler. This work was financially supported by the Deutsche Forschungsgemeinschaft, Sonderforschungsbereich 404. We acknowledge the access to computing resources at the research center Jülich and the federal computer center HWW in Stuttgart.

References

1. D. J. Jeffrey and Y. Onishi, Calculation of the resistance and mobility functions for two unequal rigid spheres in low-Reynolds-number flow. *J. Fluid Mech.* 139 (1967) 261–290.
2. G. K. Batchelor, Sedimentation in a dilute dispersion of spheres. *J. Fluid Mech.* 52 (1972) 245 pp.
3. L. Durlofsky, J. F. Brady and G. Bossis, Dynamic simulation of hydrodynamically interacting particles. *J. Fluid Mech.* 180 (1987) 21–49.
4. J. F. Brady and G. Bossis, Stokesian dynamics. *Ann. Rev. Fluid Mech.* 20 (1988) 111–157.
5. A. J. C. Ladd, Hydrodynamic interactions in a suspension of spherical particles. *J. Chem. Phys.* 88 (1998) 5051–5063.
6. A. Sangani and G. Mo, Inclusion of lubrication forces in dynamic simulations. *Phys. Fluids* 6 (1994) 1653–1662.
7. T. N. Phung, J. F. Brady, and G. Bossis, Stokesian dynamics simulation of Brownian suspensions. *J. Fluid Mech.* 313 (1995) 181–207.
8. Kim, S. and Karrila, J., *Microhydrodynamics: Principles and Selected Applications.* Boston: Butterworth-Heinemann (1991) 507 pp.
9. G. B. Jeffery, The motion of ellipsoidal particles immersed in a viscous fluid. *Proc. R. Soc. London A* 102 (1922) 161–179.
10. H. Lamb, *Hydrodynamics*, 6th edition. Cambridge/New York: Cambridge University Press/Dover (1932) 738 pp.
11. E. S. G. Shaqfeh and G. H. Fredrickson, The hydrodynamic stress in a suspension of rods. *Phys. Fluids A* 2 (1990) 7–24.
12. B. Herzhaft, E. Guazzelli, M. B. Mackaplow and E. S. G. Shaqfeh, An experimental investigation of the sedimentation of a dilute fiber Suspension. *Phys. Rev. Lett.* 77 (1996) 290–293.
13. B. Herzhaft and E. Guazzelli, Experimental study of the sedimenation of dilute and semi-dilute suspensions of fibres. *J. Fluid Mech.* 384 (1999) 133–158.
14. M. B. Mackaplow and E. S. G. Shaqfeh, A numerical study of the sedimentation of fibre suspensions. *J. Fluid Mech.* 376 (1998) 149–182.
15. I. L. Claeys and J. F. Brady, Suspensions of prolate spheroids in Stokes flow. Part 1. Dynamics of a finite number of particles in an unbounded fluid. *J. Fluid Mech.* 251 (1993) 411–442.
16. I. L. Claeys and J. F. Brady, Suspensions of prolate spheroids in Stokes flow. Part 2. Statistically homogeneous dispersions. *J. Fluid Mech.* 251 (1993) 443–477.
17. M. Sugihara-Seki, The motion of an elliptical cylinder in channel flow at low Reynolds numbers. *J. Fluid Mech.* 257 (1993) 575–596.
18. J. Feng and D. D. Joseph, The unsteady motion of solid bodies in creeping flows. *J. Fluid Mech.* 303 (1995) 83–102.
19. J. Feng, H. H. Hu and D. D. Joseph, Direct simulation of initial value problems for the motion of solid bodies in a newtonian fluid. Part 1. Sedimentation. *J. Fluid Mech.* 261 (1994) 95–134.
20. A. Ladd, Numerical Simulations of particulate suspensions via a discretized Boltzmann equation. Part 1, Theoretical foundation. *J. Fluid Mech.* 271 (1994) 285–309.
21. C. K. Aidun, Y. Lu and E.-J. Ding, Direct analysis of particulate suspensions with inertia using the discrete Boltzmann equation. *J. Fluid Mech.* 373 (1998) 287–311.

22. J. Feng, D. D. Joseph, R. Glowinski and T. W. Pan, A three-dimensional computation of the force and torque on an ellipsoid settling slowly through a viscoelastic fluid. *J. Fluid Mech.* 283 (1995) 1–16.
23. K. Höfler and S. Schwarzer, Navier–Stokes simulation with constraint forces: Finite-difference method for particle-laden flows and complex geometries. *Phys. Rev. E* 61 (2000) 7148–7160.
24. R. Glowinski, T. W. Pan, T. I. Hesla and D. D. Joseph, A distributed Lagrange multiplier/fictitious domain method for particulate flow. *Int. J. Multiphase Flow* 25 (1999) 755–794.
25. G. H. Ristow, Tumbling motion of elliptical particles in viscous two-dimensional fluids. *Int. J. Mod. Phys. C* 12 (2000) 127–139.
26. A. L. Fogelson and C. S. Peskin, A fast numerical method for solving the three-dimensional Stokes equations in the presence of suspended particles. *J. Comp. Phys.* 79 (1988) 50–69.
27. R. Peyret and T. D. Taylor, *Computational Methods for Fluid Flow.* Springer Series in Computational Physics. Berlin: Springer (1983) 358 pp.
28. C. Pozrikidis, *Introduction to Theoretical and Computational Fluid Dynamics.* New York: Oxford Univeristy Press (1997) 675 pp.
29. J. W. Perram and M. S. Wertheim, Statistical mechanics of hard ellipsoids. I. Overlap algorithm and the contact function. *J. Chem. Phys.* 58 (1985) 409–416.
30. J. W. Perram, J. Rasmussen, E. Præstgaard and J. L. Lebowitz, Ellipsoid contact potential: theory and relation to overlap potentials. *Phys. Rev. E* 54 (1996) 6565–6572.
31. P. Y. Huang, H. H. Hu and D. D. Joseph, Direct simulation of the sedimentation of elliptic particles in Oldroyd-B fluids. *J. Fluid Mech.* 362 (1998) 297–325.
32. J. Happel and H. Brenner, *Low Reynolds Number Hydrodynamics*. Englewood Cliffs, New Jersey: Prentice Hall (1965) 553pp.
33. H. Hasimoto, On the periodic fundamental solutions of the Stokes equations and their application to viscous flow past a cubic array of spheres. *J. Fluid Mech.* 5 (1959) 317–328.
34. D. L. Koch and E. S. G. Shaqfeh, The instability of a suspension of sedimenting spheroids. *J. Fluid Mech.* 209 (1989) 521–542.